

# Doping and characterization of impurity atoms in Si and Ge nanowires

Naoki Fukata\*

International Center for Materials Nanoarchitectonics, National Institute for Materials Science (NIMS), 1-1 Namiki, Tsukuba, Japan

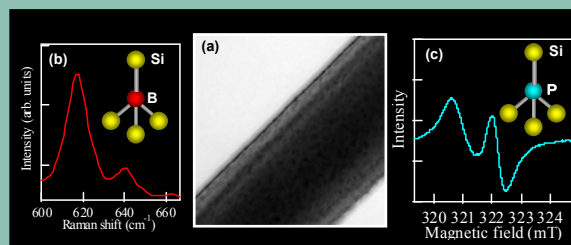
Received 29 April 2013, revised 22 September 2013, accepted 20 December 2013

Published online 3 February 2014

**Keywords** nanowire, silicon, germanium, doping, Raman scattering, electron spin resonance

\* e-mail FUKATA.Naoki@nims.go.jp, Phone: +81 29 860 4769, Fax: +81 29 860 4794

Si and Ge nanowires (SiNWs and GeNWs) are of great interest due to their novel physical properties. They are considered to be desirable materials for the next-generation metal-oxide semiconductor field-effect transistors (MOSFETs) and solar cells. Impurity doping is one of the important techniques to functionalize SiNWs and GeNWs. The crucial point is how the states of impurity atoms can be clarified. In order to realize it, we applied Raman scattering, electron spin resonance, and x-ray diffraction methods. These results showed that B and P atoms were doped and electrically activated in SiNWs and GeNWs, showing the formation of p-type and n-type NWs. Recently, Si/Ge and Ge/Si core-shell NWs were grown and the site-selective doping was demonstrated.



(a) A TEM image of Si nanowires. (b) Raman spectrum observed for B-doped Si nanowires and (c) ESR signal observed for P-doped Si nanowires.

© 2014 WILEY-VCH Verlag GmbH & Co. KGaA, Weinheim

**1 Introduction** Impurity doping is one of the most important techniques to functionalize semiconducting silicon and germanium nanowires (SiNWs and GeNWs) for the application to next-generation field effect transistors, sensors, and solar cells, and so on [1–6]. Impurity doping of SiNWs and GeNWs is generally performed *in situ* during vapor-liquid-solid (VLS) growth, which has the advantage of not inducing defects [7–16]. However, there are also certain disadvantages, such as surface doping and tapering structures created by sidewall growth, resulting in non-uniform doping along the growth direction of NWs [15, 17]. On the other hand, ion implantation is now commonly used in semiconductor manufacturing. This technique allows the precise control of dopant concentration and provides uniformity in the growth direction. Recently, ion implantation has also been performed in SiNWs to fabricate p- and n-type SiNW FETs [18–24].

In order to control the impurity doping in semiconducting NWs, characterization techniques become more and more important. Until now, various methods have been

used for the characterization of impurity atoms in semiconducting NWs [25–34]. We mainly applied Raman scattering, electron spin resonance (ESR), and x-ray diffraction (XRD) methods to clarify the bonding states and electrical activities of impurity atoms such as boron (B) and phosphorus (P) atoms in SiNWs and GeNWs [24, 29–31, 34].

In this review article, we briefly show our recent studies about impurity doping in SiNWs and GeNWs during the growth and by ion implantation. In addition to these, we also show the results of growth and site-selective doping in Si/Ge and Ge/Si core-shell NWs.

## 2 Sample preparation and characterization methods

**2.1 Sample preparation** SiNWs were synthesized by a catalytic laser ablation method. Laser ablation was performed using a frequency-doubled Nd:YAG laser (532 nm, 7 ns pulse width, 10 Hz, 150 mJ/pulse). For avoiding the effects of Si optical phonons from the Si substrate, SiNWs were directly deposited on a SiO<sub>2</sub> substrate for the

micro-Raman scattering measurements. B or P-doped SiNWs were synthesized at 1200 °C in flowing argon (Ar) gas at 50 sccm by laser ablation of a Si target with nickel (Ni) as the metal catalyst and B and P as dopants. We used four different kinds of targets:  $\text{Si}_{89}\text{Ni}_1\text{B}_{10}$ ,  $\text{Si}_{98}\text{Ni}_1\text{B}_1$ ,  $\text{Si}_{90}(\text{Ni}_2\text{P})_{10}$ , and  $\text{Si}_{99}(\text{Ni}_2\text{P})_1$ . To synthesize SiNWs codoped with both B and P, two targets were placed side-by-side and the centers of the two targets [ $\text{Si}_{98}\text{Ni}_1\text{B}_1$  and  $\text{Si}_{99}(\text{Ni}_2\text{P})_1$ ] ablated.

On the other hands, GeNWs and core-shell NWs were synthesized by a chemical vapor deposition (CVD) method. The background pressure in our CVD chamber was about  $2 \times 10^{-6}$  Pa. GeNWs were grown on a Si(111) substrate at 300–350 °C using 10 sccm of  $\text{GeH}_4$  (100%). The total pressure was set at 8 Torr by mixing with  $\text{N}_2$  gas. Doping with B and P was performed during the growth. Diborane (1%  $\text{B}_2\text{H}_6$  in  $\text{H}_2$ ) was used for the p-type dopant and phosphine (1%  $\text{PH}_3$  in  $\text{H}_2$ ) for the n-type dopant. Gold nanocolloid particles 3 nm in diameter were used as seeds for vapor-liquid-solid (VLS) growth of GeNWs. Core-shell Si/Ge and Ge/Si nanowires were grown on a Si (111) substrate using 19 sccm of  $\text{SiH}_4$  (100%) and 10 sccm  $\text{GeH}_4$  (100%), respectively. The detailed growth conditions have been reported elsewhere [34].

Impurity doping in SiNWs was also done by ion implantation after the growth. SiNWs were implanted with 30 keV  $^{11}\text{B}^+$  ions at doses ranging from  $1 \times 10^{13}$  to  $1 \times 10^{16} \text{ cm}^{-2}$ . SiNWs were also implanted with 80 keV  $\text{P}^+$  ions at the same doses. We selected the ion energy that would introduce impurity atoms into all SiNWs deposited on the substrates. These implanted SiNWs samples were annealed in an Ar gas atmosphere at 500–1000 °C for 30 minutes to electrically activate the dopant atoms.

**2.2 Characterization methods** Micro-Raman scattering measurements were performed to investigate the states of dopant atoms in NWs at room temperature with a 100x objective and a 532-nm excitation light. We also performed Raman measurements with 364-nm and 633-nm excitation lights to prove Fano interference. The spectral resolution of all data was about  $0.2\text{--}0.3 \text{ cm}^{-1}$ . The excitation power was set to be about 0.02 mW to avoid local heating effects due to the excitation Raman laser [35, 36]. ESR measurements were carried out at 4.2 K using an X-band ESR spectrometer with a magnetic field modulation of 100 kHz to investigate the state of P donors and defects in the SiNWs. X-ray diffraction (XRD) measurements using Cu K $\alpha$  radiation were performed to investigate individually the stress in the core and shell regions. Scanning electron microscopy (SEM) and transmission electron microscopy (TEM) were used to observe the SiNWs and to investigate the details of their structures. Energy-dispersive X-ray analysis (EDX) measurements were also performed during TEM to investigate the chemical content of the core-shell NWs.

**3 Growth controls of SiNWs and GeNWs** The representative SEM and TEM images of SiNWs and GeNWs are shown in Fig. 1. SiNWs were grown by both laser ablation (Fig. 1(a)) and CVD methods (Fig. 1(b)–(d)). The Si lattice fringes are clearly seen inside the SiNW, showing that the core comprises crystalline Si. The SiNW is sheathed with an amorphous  $\text{SiO}_x$  ( $x \leq 2$ ) layer. The average Si core diameter of SiNWs was about 10–15 nm in the case of laser ablation and 40 nm in the case of CVD methods. The main growth direction was [111].

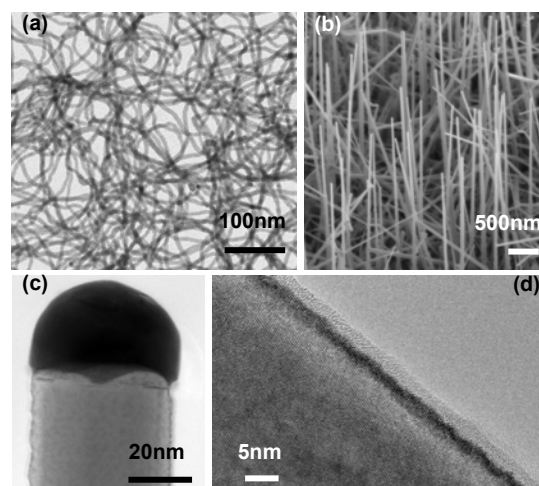


**Figure 1** Representative SEM images of SiNWs synthesized by (a) laser ablation and (b) CVD methods. (c) Low- and (d) high-resolution TEM images of SiNWs synthesized by CVD methods.

GeNWs were grown by the same CVD method as SiNWs. The GeNWs are also covered with oxide layer and the diameter is about 10–20 nm including surface oxide layer as shown in Fig. 2(a). The crystallinity of GeNWs was also checked by TEM (Fig. 2(b)). The main growth direction is [110] for GeNWs with diameter smaller than about 20 nm, and [111] for GeNWs with diameter larger than 20 nm. This is the same tendency as has been observed in SiNWs [37, 38].

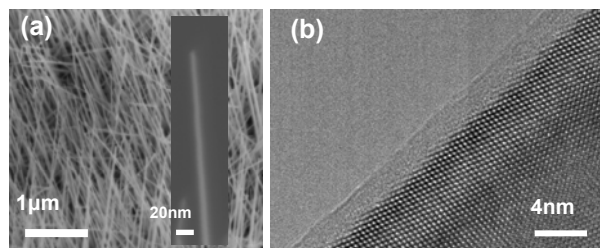


**Figure 2** (a) Representative SEM images of GeNWs synthesized by CVD methods. (b) A high-resolution TEM image of GeNWs synthesized by CVD methods.

## 4 Impurity doping

### 4.1 Impurity doping in SiNWs during growth

The result of Raman scattering measurements for B-doped SiNWs are shown in Fig. 3(a). The intense peak at about  $519.0\text{ cm}^{-1}$  is due to the Si optical phonon peak. The peak position is lower than that for bulk Si. The peak also shows an asymmetric broadening toward lower wavenumbers. These can be well explained by the phonon confinement effect [35, 36, 39–41]. Two peaks at about  $618$  and  $640\text{ cm}^{-1}$  are shown for B-doped SiNWs (Fig. 3(b)). The peak frequencies are in good agreement with the  $^{11}\text{B}$  ( $620\text{ cm}^{-1}$ ) and  $^{10}\text{B}$  ( $643\text{ cm}^{-1}$ ) local vibrational peaks in B-doped bulk Si [42]. The ratio of these peak intensities is estimated as being roughly 4:1, which is also in good agreement with the natural abundance of the two isotopes of  $^{11}\text{B}$  (80.2%) and  $^{10}\text{B}$  (19.8%) [42]. Based on these results, these two peaks can be assigned to the local vibrational modes of B in SiNWs [29, 30]. This demonstrates that B atoms have been doped in substitutional sites of the crystalline Si core of SiNWs during laser ablation. The same results have been obtained for SiNWs synthesized by the CVD method.

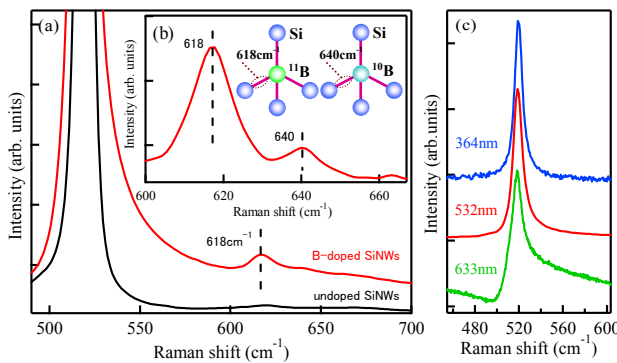


**Figure 3** (a) Optical phonon peaks of the SiNWs synthesized using a  $\text{Si}_{89}\text{Ni}_1\text{B}_{10}$  target (B-doped SiNWs) and a  $\text{Si}_{99}\text{Ni}_1$  target (undoped SiNWs) measured by micro-Raman scattering measurements. (b) Magnification of the Raman peak observed for B-doped SiNWs. (c) Dependence of the line shapes of the Si optical phonon peak on the excitation wavelength. Reproduced from Ref. [29].

The optical phonon peak for B-doped SiNWs showed a large broadening to higher wavenumbers with increasing excitation wavelength during Raman measurements (Fig. 3(c)). The phonon peak observed at 633-nm excitation clearly showed antiresonance at low wavenumber side. These line shapes are the characteristics of the Fano effect [43–46]. This broadening is due to coupling between discrete optical phonons and the continuum of interband hole excitations in degenerately doped p-type Si [43–46]. The Fano effect shows B atoms are electrically activated in SiNWs. Based on these results, the formation of p-type SiNWs is demonstrated. The electrical active B concentration was estimated by the Fano equation. The Fano equation is given by

$$I(\omega) = I_0 \frac{(q + \varepsilon)^2}{(1 + \varepsilon^2)}, \quad (1)$$

where  $\omega$  is the wavenumber,  $I_0$  the prefactor,  $q$  the asymmetry parameter, and  $\varepsilon$  is given by  $\varepsilon = (\omega - \omega_p)/\Gamma$ , where  $\omega_p$  is the phonon wavenumber and  $\Gamma$  is the linewidth parameter. The electrical active B concentration in SiNWs can be roughly estimated to be in the order of  $10^{19}\text{ cm}^{-3}$  from the fitting by the Fano equation. However, Fano effect gives no information about the electrically inactive B concentration.

ESR measurements were performed to investigate the status of P atoms in SiNWs. Figure 4 shows typical results of ESR measurements for P-doped SiNWs synthesized using the  $\text{Si}_{90}(\text{Ni}_2\text{P})_{10}$  targets. The ESR signal observed for P-doped SiNWs is deconvoluted to at least two components with g-values of 1.998 and 2.005–2.006. The ESR signal at 2.005–2.006 is attributable to interfacial defects between the surface oxide and crystalline Si core of SiNWs, which are so-called  $P_b$  centers [47–51]. This is the well known defects in bulk Si. The g-value of 1.998 corresponds to that of conduction electrons in Si [30, 31, 52, 53], indicating that the ESR signal can be attributed to the conduction electrons in the Si core of the SiNWs. This result clearly demonstrates that P atoms were doped in substitutional sites of the crystalline Si core of SiNWs during laser ablation, resulting in the formation of n-type P-doped SiNWs. The electrical active P concentration was estimated to be in the order of  $10^{19}\text{ cm}^{-3}$  from the analysis of ESR signal [31]. The same results have been obtained for SiNWs synthesized by the CVD method.

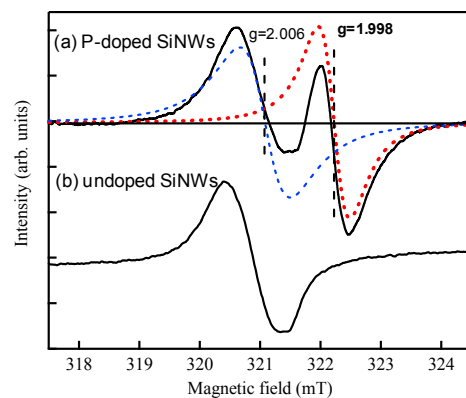


**Figure 4** ESR spectra observed for undoped and P-doped SiNWs synthesized using  $\text{Si}_{90}(\text{Ni}_2\text{P})_{10}$  targets. Reproduced from Ref. [31].

**4.2 Impurity doping in SiNWs by ion implantation** In bulk Si, the introducing of dopant impurities and defects, their interaction, the recrystallization process with defect annihilation in implanted regions, and the subsequent reactivation process of dopant impurities have been



extensively investigated. The recrystallization process with defect annihilation is a key point for controlling the reactivation and distribution of dopant atoms.

Ion implantation was performed as shown in Fig. 5(a). The depth profiles of B and P atoms in bulk Si, simulated by using TRIM are shown in Fig. 5(b). Similarly to the case for bulk Si, the concentration of impurity atoms implanted into SiNWs changes depending on the distance from the substrate. Therefore, the TEM images of the most damaged SiNWs for each implantation doses are shown in this paper. The typical high-resolution TEM image of B-implanted SiNW after an activation annealing at 900 °C is shown in Fig. 5(c). The implantation dose is  $1 \times 10^{16} \text{ B}^+/\text{cm}^2$ . The Si lattice fringes have clearly been reappeared in the Si core region, but the structure is polycrystal, not single-crystal, indicating that nucleation occurs randomly in Si core of SiNWs. Figure 5(d) shows the result of P-implanted SiNWs. The implantation dose is  $5 \times 10^{15} \text{ P}^+/\text{cm}^2$ . The Si lattice fringes were not clearly visible, and the surface roughness was significantly higher than the B-implanted case. In the case of B implantation, the core changed to polycrystal at doses exceeding  $1 \times 10^{16} \text{ cm}^{-2}$ , while for P implantation, polycrystal structures occur at doses above  $1 \times 10^{14} \text{ cm}^{-2}$ . These are due to the greater damage caused by P implantation, since the mass of P is greater than that of B.

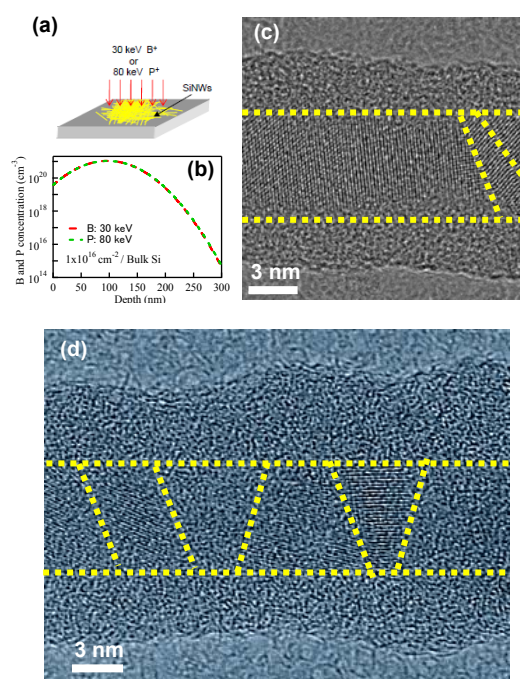


**Figure 5** (a) Illustration of ion implantation for SiNWs. (b) The depth profiles of B and P as estimated by TRIM. Typical TEM images of SiNW after ion implantation with doses of (c)  $1 \times 10^{16} \text{ B}^+/\text{cm}^2$  and (d)  $5 \times 10^{15} \text{ P}^+/\text{cm}^2$ . The activation annealing of dopant atoms was performed at 900 °C after implantation. Reproduced from Ref. [24].

Raman and ESR measurements were performed to investigate the recrystallization and reactivation of dopant atoms after the ion implantation and the following the activation annealing. After the activation annealing, the  $^{11}\text{B}$  local vibrational peak and the Fano broadening in the Si optical phonon peak were observed for B-implanted, while the conduction electron signal was observed for P-implanted SiNWs [24]. However, the activation rates for B-implanted and P-implanted SiNWs were 1–10%. The low activation ratio is due to the formation of polycrystal structure and the compensation by residual defects [24].

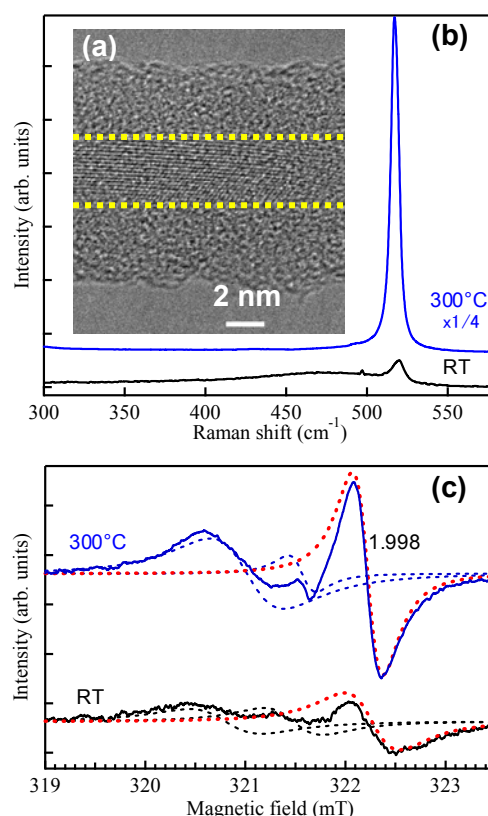


**Figure 6** (a) A TEM image of the SiNW after hot implantation at 300 °C. (b) Raman spectra and (c) ESR signals observed for SiNWs implanted with  $1 \times 10^{15} \text{ P}^+/\text{cm}^2$  at RT and 300 °C. Activation annealing was performed at 900 °C. Reproduced from Ref. [24].

To suppress the formation of polycrystals and improve the activation rate of dopant atoms, ion implantation was performed at 300 °C for P-implanted SiNWs. This process is generally called by hot implantation. The TEM image is shown in Fig. 6(a). The Si lattice fringes clearly show the reformation of single-crystal in SiNWs as a result of hot implantation. The intensity of the Si optical phonon peak significantly increased for the hot-implanted sample, as shown in Fig. 6(b). The ESR signal intensity of conduction

electrons also becomes significantly larger in hot implantation than in ordinary implantation at RT as shown in Fig. 6(c). This result clearly shows hot implantation to be a very useful method for realizing heavy ion implantation at high doses in SiNWs.

#### 4.3 Impurity doping in GeNWs during growth

Ge is considered to be a more desirable material for the next-generation MOSFETs since both electron and hole mobilities in Ge are higher than those in Si. Until now, GeNWs have been grown by various methods to control the growth and shape, and the electrical properties have been comprehensively investigated [13, 54–61].

Micro-Raman scattering measurements were also applied for GeNWs. The results of B-doped GeNWs are shown in Fig. 7. The intense peak at about 300.2 cm<sup>-1</sup> for bulk-Ge is due to the Ge optical phonon peak. Two peaks at about 544 and 565 cm<sup>-1</sup> were observed for B-doped GeNWs. The intensity increased with increasing B<sub>2</sub>H<sub>6</sub> gas ratio [62]. The intensity ratio of the peak at 544 cm<sup>-1</sup> to that at 565 cm<sup>-1</sup> is roughly estimated to be about 4:1 after removing the effect of the second-order Ge optical phonon peak at around 570 cm<sup>-1</sup>. The intensity ratio is in good agreement with the natural abundance of the two isotopes of <sup>11</sup>B (80.2%) and <sup>10</sup>B (19.8%). If Si atoms were replaced by Ge atoms, the B local vibrational peaks shifted to around 540–580 cm<sup>-1</sup>. The peaks at about 544 and 565 cm<sup>-1</sup> are in this frequency range. Based on the dependence on the B<sub>2</sub>H<sub>6</sub> gas ratio and the peak position, the peak at 544 cm<sup>-1</sup> can be assigned to the <sup>11</sup>B local vibrational peak in

GeNWs, while the peak at 565 cm<sup>-1</sup> can be assigned to the overlapping peak of the <sup>10</sup>B local vibrational peak and the second-order Ge optical phonon peak. These B local vibrational peaks have never been reported even for bulk Ge.

The optical phonon peak observed for undoped GeNWs showed a downshift and a broadening toward lower wavenumbers compared with the case of bulk Ge. This is due to the phonon confinement effect caused by the small diameter of GeNWs [35, 36, 39–41] as well as the case of SiNWs. The downshift and asymmetric broadening toward lower wavenumber became more pronounced with increasing B<sub>2</sub>H<sub>6</sub> gas ratio. This is attributable to the Fano interference, which is due to coupling between discrete optical phonons and the continuum of interband hole excitations in degenerately doped p-type Ge [43–46]. The electrical active B concentration in GeNWs can be roughly estimated to be in the order of 10<sup>19</sup> cm<sup>-3</sup> from the fitting by the Fano equation [62].

The results of Raman scattering measurements for P-doped GeNWs are shown in Fig. 8. A new peak was observed at about 342–345 cm<sup>-1</sup>. The peak intensity increased with increasing PH<sub>3</sub> gas ratio. The frequency of the P local vibrational peak can be roughly estimated to be around 360 cm<sup>-1</sup> in a similar way to the estimation of the B local vibrational peaks for B-doped GeNWs. The estimated value is in good agreement with the experimental value of 342–345 cm<sup>-1</sup>. Based on these considerations, the peak at 342–345 cm<sup>-1</sup> can be assigned to the local vibrational peak of P in GeNWs [58]. The P local vibrational peaks have also never been reported even for bulk Ge.

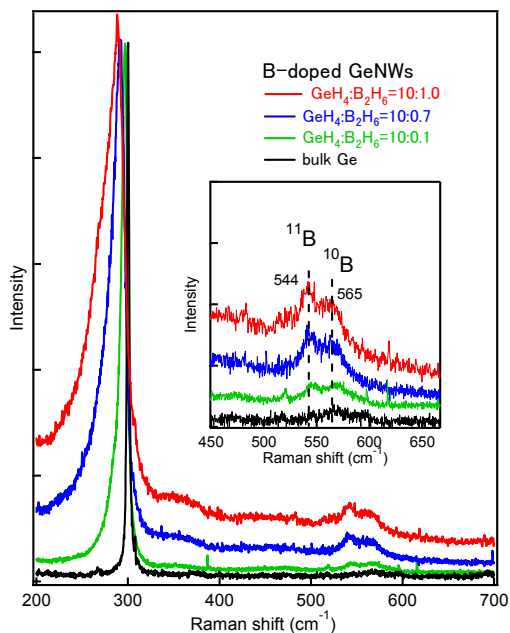


**Figure 7** Raman spectra observed for B-doped GeNWs (B<sub>2</sub>H<sub>6</sub> flux of 1.0, 0.7, and 0.1), and bulk Ge. The inset shows the magnification of the Raman spectra ranging from 200 to 700 cm<sup>-1</sup>. Reproduced from Ref. [62].

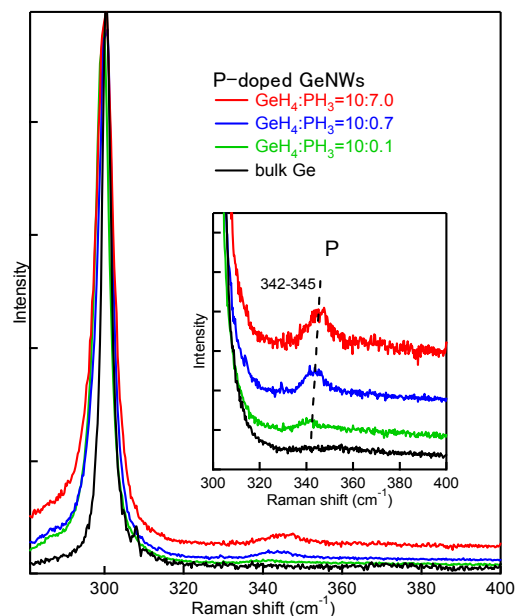


**Figure 8** Raman spectra observed for P-doped GeNWs (PH<sub>3</sub> flux of 7.0, 0.7, and 0.1), and bulk Ge. The inset shows the magnification of the Raman spectra ranging from 200 to 700 cm<sup>-1</sup>. Reproduced from Ref. [62].

The downshift and asymmetric broadening toward lower wavenumbers became more pronounced with increasing  $\text{PH}_3$  gas ratio similar to the case observed for B-doped GeNWs. This also can be well explained by the Fano effect, showing the electrical activity of P atoms in GeNWs and finally the formation of n-type GeNWs. The electrical active P concentrations were estimated to be in the order of  $10^{19} \text{ cm}^{-3}$  from the fitting by the Fano equation [62].

It is important to clarify whether the doping of B and P are mainly due to core doping or shell doping. Therefore, it is necessary to investigate the distribution of dopant atoms in axial and radial directions of NWs. Recently, the inhomogeneous distributions of dopant atoms in SiNWs and GeNWs have been investigated by atom probe measurements and electrical measurements [17, 27, 63]. The dopant atoms tend to distribute near the surface region due to the surface doping created by sidewall growth. In order to clarify the effect of shell doping, position dependent Raman measurements were performed for the top and bottom regions of B- or P-doped GeNWs grown at the edge of the Si substrate as shown in Fig. 9. We precisely scanned the laser light from the top to the bottom by using a micrometer of the specimen stage during Raman measurements. The numbers of GeNWs are different by location. To remove the effect, the intensity of B and P local vibrational peaks were normalized by the Ge optical phonon peak. The

intensity of B local vibrational peak shown in Fig. 9(b) does not show big differences up to the  $\text{B}_2\text{H}_6$  gas flux of 0.4 sccm, while the intensity of the bottom region is slightly larger than that of the top region at 0.7 sccm, finally the former is clearly larger than the latter at 1.0 sccm. This means that the shell doping has to be considered from the  $\text{B}_2\text{H}_6$  gas flux more than 0.7 sccm. On the other hand, the intensity of P local vibrational peak does not show big differences (Fig. 9(c)), meaning that the P doping is mainly due to core doping for P-doped GeNWs.

**4.4 Impurity doping in Si/Ge and Ge/Si core-shell NWs** The retardation of carrier mobility due to impurity scattering has to be taken into account when doping the channel region. Core-shell NWs using Si and Ge show potential for suppression of impurity scattering and numerous studies have been carried out, both experimentally and theoretically [64–74]. Recently, the author reported the growth of four different types of Si/Ge and Ge/Si core-shell NWs and selective doping in the core and shell regions [34].

Four different types of Si/Ge (i-Si/n-Ge, p-Si/i-Ge) and Ge/Si (n-Ge/i-Si, i-Ge/p-Si) core-shell NWs were prepared by CVD. Here, i-Si means intrinsic Si. The representative EDX image of i-Si/n-Ge core shell NWs is shown in Fig. 10. The image clearly shows the construction of Si and Ge core shell nanostructures.

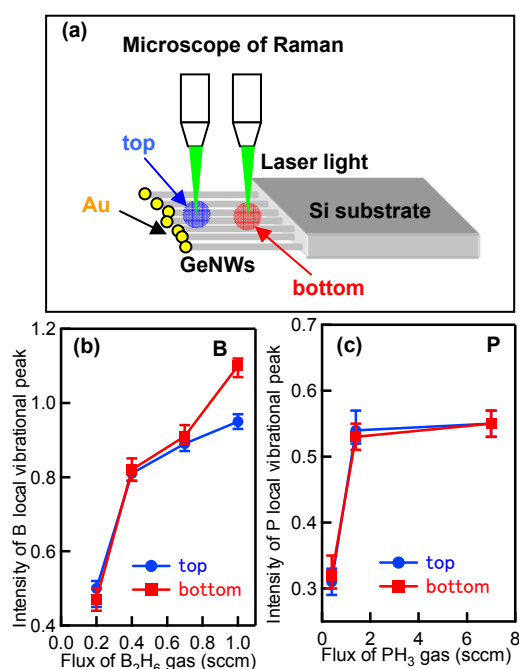


**Figure 9** (a) Illustration of Raman measurements of GeNWs grown at the edge of Si substrate. Dependences of (b) the intensity of B local vibrational peak on the flux of  $\text{B}_2\text{H}_6$  gas and (c) the intensity of P local vibrational peak on the flux of  $\text{PH}_3$  gas. Reproduced from Ref. [62].

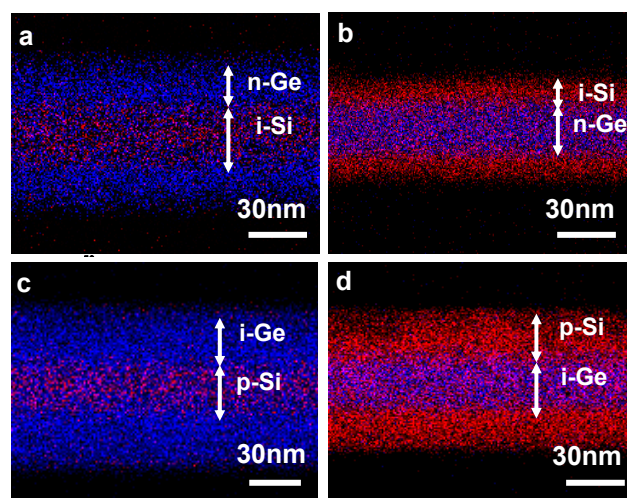


**Figure 10** EDX images of (a) i-Si/n-Ge, (b) n-Ge/i-Si, (c) p-Si/i-Ge, and (d) i-Ge/p-Si core-shell NWs. Reproduced from Ref. [34].

The selective doping in core and shell regions in Si/Ge and Ge/Si core-shell NWs were demonstrated by Raman scattering measurements of the local vibrational modes of dopant atoms and the Fano effect in the optical phonon peaks (Fig. 11). The results of Raman measurements of the n-Ge shell in i-Si/n-Ge core-shell NWs are shown in Fig. 11(a). A peak was observed at about  $345 \text{ cm}^{-1}$  in addition to the Ge optical phonon peak at around  $300 \text{ cm}^{-1}$  (Fig.



11(b)). The peak position coincides with that of the P local vibrational mode in GeNWs [62], showing that the peak can be assigned to the P local vibrational peak from the Ge shell and that the P atoms have been doped into the substitutional sites of Ge atoms in the Ge region. The Ge optical phonon peak show a slightly asymmetric broadening toward lower wavenumbers, most likely resulting from the Fano effect [43-45, 62]. The observation of the local vibrational peak and the Fano effect demonstrate the selective doping in the shell region, resulting in the formation of the n-Ge shell for i-Si/n-Ge core-shell NWs. The same experiments were performed for i-Ge/p-Si core-shell NWs. Two peaks were observed at about 618 and 640  $\text{cm}^{-1}$  as shown in Fig. 11(f). These are assigned to the local vibrational modes of the two isotopes of  $^{11}\text{B}$  (80.2%) and  $^{10}\text{B}$  (19.8%) in the Si [29, 42], showing that the B atoms have been doped into the substitutional sites of Si atoms in the Si shell region. The Si optical phonon peak shows a asymmetric broadening to higher wavenumbers, which is due to the Fano effect [43-45, 62]. These results clearly show the selective doping in the shell region, resulting in the formation of p-Si shell for i-Ge/p-Si core-shell NWs.

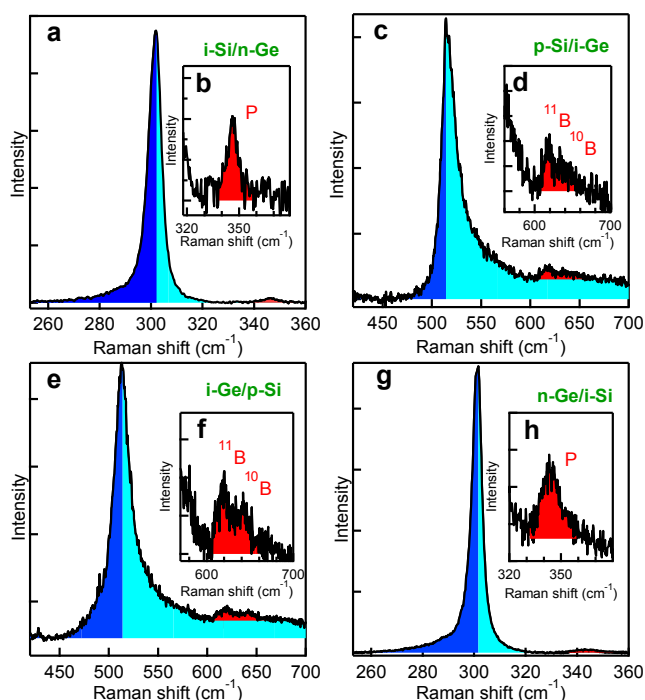


**Figure 11** Raman spectra observed for (a) i-Si/n-Ge, (c) p-Si/i-Ge, (e) i-Ge/p-Si, and (g) n-Ge/i-Si core-shell NWs. Insets (b) and (h) are the magnification of the P local vibrational mode in the n-Ge shell layer and the n-Ge core, respectively. Insets (d) and (f) are the magnification of the  $^{11}\text{B}$  and  $^{10}\text{B}$  local vibrational peaks in the p-Si core and the p-Si shell layer, respectively. The shell growth time is 15 min. Reproduced from Ref. [34].

As for impurity doping in the core regions, Raman measurements were performed before the shell growth. The results of B doping in SiNWs and P doping in GeNWs are shown in Fig. 11c, 11d, 11g, and 11h. The local vibrational peaks of B in Si and P in Ge were clearly observed. Asymmetric broadening due to the Fano effect were also observed. These results demonstrate the formation of p-Si core and n-Ge core NWs. Based on these results, the site selective doping in Si/Ge and Ge/Si core-shell NWs was demonstrated.

The values of  $q$  and  $\Gamma$  were estimated to be about  $-18.0$  and  $2.8$ , respectively, for i-Si/n-Ge. On the other hand, the values of  $q$  and  $\Gamma$  were estimated to be about  $8.8$  and  $10.5$ , respectively, for i-Ge/p-Si. From our previous results for P-doped GeNWs [62] and typical results for B-doped bulk Si [75-77], the electrically active P and B concentration in the Ge and Si shells can be roughly estimated to be in the order of  $10^{19} \text{ cm}^{-3}$ .

The dopant distribution is also important for device applications such as MOSFETs. The dopant atoms uniformly distribute in the axial direction in the core regions if the structures of NWs are untapered [62]. The core-shell NWs shown in Figs. 10 and 11 are untapered in the axial growth direction, showing that the axial distribution of dopant atoms is probably almost uniform. On the other hand, the situation is different for the radial direction. The dopant atoms distribute in the radial direction preferentially near surface regions [78]. However, this is probably not a serious problem from the view point of introducing carriers from the core to the shell regions. As for the shell regions, dopant atoms must be inhomogeneously distributed in the radial direction due to the effect of stress. Considering future device applications to MOSFETs, the thickness of the shell layers should be thin. Therefore the dopant distribution in the radial direction also may not be a serious problem.

The dopant diffusion and the Si-Ge interdiffusion in core-shell NWs are also important subjects. If core-shell NWs are being considered for use in nano-devices, this interdiffusion of Si and Ge, and that of dopant atoms will be crucial problems, since they affect the abruptness of the band offset at the Si/Ge interface. Considering the diffusion constants of B and P in Si and Ge, the effects of dopant diffusion in the Ge/Si core-shell NWs are almost negligible [62, 79-89]. The dopant diffusion in the Si/Ge core-shell NWs is much more difficult than in the abovementioned Ge/Si core-shell NWs because the shell growth temperature is  $600^\circ\text{C}$  for the Si/Ge core-shell NWs, lower than that of the Ge/Si core-shell NWs. Hence, the dopant diffusion is close to zero in both cases. However, the interdiffusion of Si and Ge during the shell growth process at  $700^\circ\text{C}$  should be taken into account. Considering the diffusion coefficients of Ge in Si and Si in Ge, the diffusion of Ge atoms into Si is virtually zero, while it is possible for Si atoms to diffuse as far as  $10 \text{ nm}$  at  $700^\circ\text{C}$  in  $15 \text{ min}$  [90-92]. Hence, the intermixing of Si and Ge might occur, but only at the interface of the Ge/Si core-shell NWs.

**5 Segregation behaviors of impurity atoms in SiNWs** The behaviors of dopant atoms after doping are not yet fully understood. In order to clarify the segregation behaviors of dopant impurities in SiNWs during thermal oxidation, the above-mentioned same techniques, Raman scattering measurements and ESR measurements were applied.

Thermal oxidation thickens the surface oxide layer, resulting in a decrease in the diameter of the Si core of SiNWs (inset of Fig. 12). The dependence of the peak intensity of  $^{11}\text{B}$  local vibrational peak and the ESR signal from conduction electrons on annealing time in oxygen are summarized in Fig. 12. The results show that B atoms segregate much faster than P atoms. In bulk Si, the segregation of P and B atoms at the Si/SiO<sub>2</sub> interface has been studied [93, 94]. The results showed that B atoms preferentially segregate in SiO<sub>2</sub>, while P atoms pile up at the Si surface. The results for SiNWs show the similar segregation behaviors as those obtained in bulk Si. The enhanced B diffusion during oxidation is a possible reason for the fast segregation of B atoms. Silicon self-interstitials are generated at the Si/SiO<sub>2</sub> interface during oxidation [95–98]. The Si self-interstitials can easily diffuse into Si crystalline region and effectively interact with B atoms in deeper region, finally enhance the B diffusion [95–100].

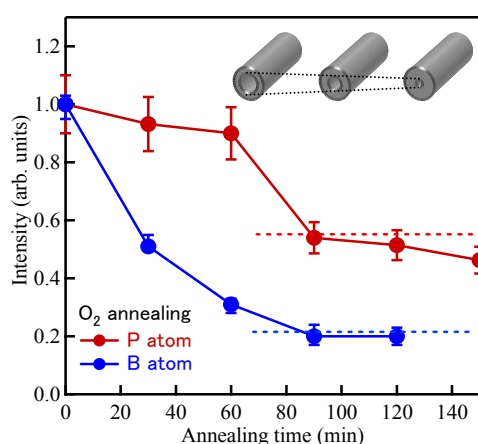


**Figure 12** Dependence of the peak intensity of  $^{11}\text{B}$  local vibrational peak and the ESR signal from conduction electrons on annealing time in O<sub>2</sub>. Reproduced from Ref. [78].

In order to further confirm the result obtained in Fig. 12, the same experiments were performed for B- and P-codoped SiNWs. The Si optical phonon peak observed for codoped SiNWs does not show Fano broadening, indicating compensation by P donors [101]. The peak intensity of B local vibrational peak was decreased by thermal oxidation at 900 °C (Fig. 13(a)). This is due to the segregation of B to the surface oxide layer. No ESR signal from conduction electrons was observed in codoped SiNWs, showing compensation by B acceptors (Fig. 13(b)). However, the signal of conduction electrons was observed after thermal

oxidation at 900 °C (Fig. 13(b)). The oxidation behaviors show a clear inverse correlation between B and P (Fig. 13(c)). Observations of the ESR signal from conduction electrons show that P donors compensated by B acceptors were electrically reactivated by the segregation of B. This result clearly demonstrates that B atoms preferentially segregate in SiO<sub>2</sub>, while P atoms pile up at the Si surface.

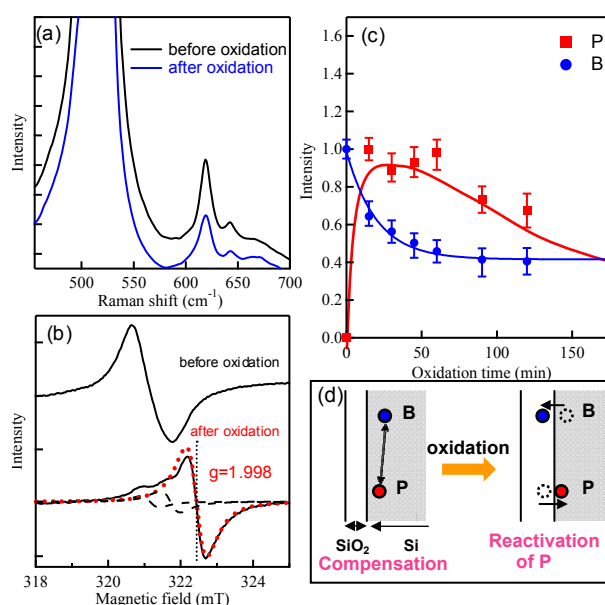


**Figure 13** (a) Thermal oxidation behaviors of the Si optical phonon peak and the B local vibrational peak observed by Raman scattering measurements and (b) that of the ESR signal observed at 4.2 K for B- and P-codoped SiNWs. Oxidation time was 30 min. (c) The dependence of the peak intensity of the B local vibrational peak and the ESR signal from conduction electrons on thermal oxidation time for B- and P-codoped SiNWs. The Si<sub>98</sub>Ni<sub>1</sub>B<sub>1</sub> and Si<sub>99</sub>(Ni<sub>2</sub>P)<sub>1</sub> targets were used to synthesize the codoped SiNWs. (d) Illustration of the difference segregation behaviors of B and P in SiNWs during thermal oxidation. Reproduced from Ref. [78].

**6 Conclusion** Impurity doping in SiNWs and GeNWs were performed during the growth by a catalytic laser ablation and CVD. The doping concentrations can be controlled by changing the growth conditions such as the composition of ablation targets, dopant gas fluxes and growth temperatures.

The status of dopant atoms, chemical bonding states and the electrical activities were clearly evaluated by Raman scattering and ESR measurements. The former method is useful for B in SiNWs and P and B in GeNWs, while the latter is useful for P in SiNWs. The local vibrational modes of dopant atoms and Fano broadening in the optical phonon peaks can be observed by Raman measurements.



The electrical active dopant concentrations can be estimated by the analysis of Fano broadening. On the other hand, the conduction electron signal can be observed by ESR measurements, showing both the chemical bonding state and the electrical activity of P donors in SiNWs.

Ion implantation techniques can be also applied for impurity doping in SiNWs. It introduces defects in SiNWs. It is necessary to investigate the recrystallization and reactivation of dopant atoms during activation annealing. At higher ion doses, the crystal structures inside of SiNWs show the polysrystal structures. In order to get single crystal and enhance the activation rate of impurity atoms, hot-implantation can be considered to be a very useful technique.

Core-shell NWs composed of Si and Ge are key structures for realizing high mobility transistor channels, since the site-selective doping and band-offset in core-shell NWs separate the carrier transport region from the impurity doped region, resulting in the suppression of impurity scattering. Four different types of Si/Ge (i-Si/n-Ge, p-Si/i-Ge) and Ge/Si (n-Ge/i-Si, i-Ge/p-Si) core-shell NWs structures were grown by CVD. The observation of boron (B) and phosphorus (P) local vibrational peaks and the Fano broadening in the optical phonon peaks clearly demonstrated that the B and P atoms are selectively doped into the shell and core regions, respectively and electrically activated in the substitutional sites, showing the success of site-selective doping.

The segregation of B and P atoms in SiNWs during annealing in oxygen was detected by micro-Raman scattering and ESR measurements. The results showed that B atoms preferentially segregate in the surface oxide layer, whereas P atoms tend to accumulate in the Si region around the interface of SiNWs.

**Acknowledgements** This work was in part supported by a Funding Program for Next Generation World-Leading Researchers (NEXT Program), Japan, and the World Premier International Research Center Initiative (WPI Initiative), MEXT, Japan. This study was also supported by the Japan Science and Technology Agency (JST). The author thanks students from University of Tsukuba for doing some parts of experiments. The author also thanks K. Mutakami, T. Sekiguchi, M. Mitome, Y. Bando, S. Hishita, M. Kirkham, J. I. Hong, Z. L. Wang, and R. Snyder for fruitful and helpful discussion.

## References

- [1] Y. Li, F. Qian and C. M. Lieber, *Mater. Today* **9**, 18 (2006).
- [2] C. Thelander, P. Agarwal, S. Brongersma, J. Eymery, L. F. Feiner, A. Forchel, M. Scheffler, W. Riess, B. J. Ohlsson, U. Gösele, and L. Samuelson, *Mater. Today* **9**, 28 (2006).
- [3] P. J. Pauzauskie and P. Yang, *Mater. Today* **9**, 36 (2006).
- [4] H. J. Fan, P. Werner, and M. Zacharias, *Small* **2**, 700 (2006).
- [5] Z. L. Wang and J. Song, *Science* **312**, 242 (2006).
- [6] R. Rurali, *Rev. Mod. Phys.* **82**, 427 (2010).
- [7] A. M. Morales and C. M. Lieber, *Science* **279**, 208 (1998).
- [8] Y. F. Zhang, Y. H. Tang, N. Wang, D. P. Yu, C. S. Lee, I. Bello, and S. T. Lee, *Appl. Phys. Lett.* **72**, 1835 (1998).
- [9] Y. Cui, X. Duan, J. Hu, and C. M. Lieber, *J. Phys. Chem. B* **104**, 5213 (2000).
- [10] K. K. Lew, L. Pan, T. E. Bogart, S. M. Dilts, E. C. Dickey, J. M. Redwing, Y. Wang, M. Cabassi, T. S. Mayer, and S. W. Novak, *Appl. Phys. Lett.* **85**, 3101 (2004).
- [11] G. Zheng, W. Lu, S. Jin, and C. M. Lieber, *Adv. Mater.* **16**, 1890 (2004).
- [12] L. Pan, K. K. Lew, J. M. Redwing, and E. C. Dickey, *J. Cryst. Growth* **277**, 428 (2005).
- [13] Y. Wang, K. K. Lew, T. T. Ho, L. Pan, S. W. Novak, E. C. Dickey, J. M. Redwing, and T. S. Mayer, *Nano Lett.* **5**, 2139 (2005).
- [14] C. Yang, Z. Zhong, and C. M. Lieber, *Science* **310**, 1304 (2005).
- [15] E. Tutuc, S. Guha, and J. O. Chu, *Appl. Phys. Lett.* **88**, 043113 (2006).
- [16] A. F. Morral, J. Arbiol, J. D. Prades, A. Cirera, and J. R. Morante, *Adv. Mater.* **19**, 1347 (2007).
- [17] D. E. Perea, E. R. Hemesath, E. J. Schwalbach, J. L. Lensch-Falk, P. W. Voorhees, and L. J. Lauhon, *Nature Nanotechnol.* **4**, 315 (2009).
- [18] A. Colli, A. Fasoli, C. Ronning, S. Pisana, S. Piscanec, and A. C. Ferrari, *Nano Lett.* **8**, 2188 (2008).
- [19] G. M. Cohen, M. J. Rooks, J. O. Chu, S. E. Laux, P. M. Solomon, J. A. Ott, R. J. Miller, and W. Haensch, *Appl. Phys. Lett.* **90**, 233110 (2007).
- [20] O. Hayden, M. T. Bjork, H. Schmid, H. Riel, U. Drechsler, S. F. Karg, E. Lortscher, and W. Riess, *Small* **3**, 230 (2007).
- [21] P. D. Kanungo, R. Kogler, K. Nguyen-Duc, N. Zakharov, P. Werner, and U. Gosele, *Nanotechnology* **20**, 165706 (2009).
- [22] P. D. Kanungo, R. Kogler, P. Werner, U. Gosele, and W. Skorupa, *Nanoscale Res. Lett.* **5**, 243 (2010).
- [23] P. D. Kanungo, R. Kogler, N. Zakharov, P. Werner, R. Scholz, and W. Skorupa, *Cryst. Growth Des.* **11**, 2690 (2011).
- [24] N. Fukata, R. Takiguchi, S. Ishida, S. Yokono, S. Hishita, and K. Murakami, *ACS Nano* **6**, 3278 (2012).
- [25] D. D. Ma, C. S. Lee, and S. T. Lee, *Appl. Phys. Lett.* **79**, 2468 (2001).
- [26] Y. H. Tang, T. K. Sham, A. Jurgensen, Y. F. Hu, C. S. Lee, and S. T. Lee, *Appl. Phys. Lett.* **80**, 3709 (2002).
- [27] E. Koren, N. Berkovitch, and Y. Rosenwaks, *Nano Lett.* **10**, 1163 (2010).
- [28] E. Koren, J. K. Hyun, U. Givan, E. R. Hemesath, L. J. Lauhon, and Y. Rosenwaks, *Nano Lett.* **11**, 183 (2011).
- [29] N. Fukata, J. Chen, T. Sekiguchi, N. Okada, K. Murakami, T. Tsurui, and S. Ito, *Appl. Phys. Lett.* **89**, 203109 (2006).
- [30] N. Fukata, *Adv. Mater.* **21**, 2829 (2009).
- [31] N. Fukata, J. Chen, T. Sekiguchi, S. Matsushita, N. Oshima, N. Uchida, K. Murakami, T. Tsurui, and S. Ito, *Appl. Phys. Lett.* **90**, 153117 (2007).
- [32] M. A. Seo, J. Yoo, S. A. Dayeh, S. T. Picraux, A. J. Taylor, and R. P. Prasankumar, *Nano Lett.* **12**, 6334 (2012).
- [33] Y. Wang, K. K. Lew, T. T. Ho, L. Pan, S. W. Novak, E. C. Dickey, J. M. Redwing, and T. S. Mayer, *Nano Lett.* **5**, 2139 (2005).

- [34] N. Fukata, M. Mitome, T. Sekiguchi, Y. Bando, M. Kirkham, J.-i. Hong, Z. L. Wang, and R. S. Snyder, *ACS Nano* **6**, 8878 (2012).
- [35] S. Piscanec, M. Cantoro, A.C. Ferrari, J. A. Zapien, Y. Lifshitz, S. T. Lee, S. Hofmann, and J. Robertson, *Phys. Rev. B* **68**, 241312(R) (2003).
- [36] N. Fukata, T. Oshima, N. Okada, T. Kizuka, T. Tsurui, S. Ito, and K. Murakami, *J. Appl. Phys.* **100**, 024311 (2006).
- [37] Y. Cui, L. J. Lauhon, M. S. Gudiksen, J. Wang, and C. M. Lieber, *Appl. Phys. Lett.* **78**, 2214 (2001).
- [38] Y. Wu, Y. Cui, L. Huynh, C. J. Barrelet, D. C. Bell, and C. M. Lieber, *Nano Lett.* **4**, 443 (2004).
- [39] S. Bhattachayya and S. Samui, *Appl. Phys. Lett.* **84**, 1564 (2004).
- [40] K. W. Adu, H. R. Gutierrez, U. J. Kim, G. U. Sumanasekera, and P. C. Eklund, *Nano Lett.* **5**, 400 (2005).
- [41] N. Fukata, T. Oshima, K. Murakami, T. Kizuka, T. Tsurui, and S. Ito, *Appl. Phys. Lett.* **86**, 213112 (2005).
- [42] C. P. Herrero and M. Stutzmann, *Phys. Rev. B* **38**, 12668 (1988).
- [43] U. Fano, *Phys. Rev.* **124**, 1866 (1961).
- [44] H. Richter, Z. P. Wang, and L. Ley, *Solid State Commun.* **39**, 625 (1981).
- [45] D. Olego and M. Cardona, *Phys. Rev.* **23**, 6592 (1981).
- [46] I. H. Campbell and P. M. Fauchet, *Sol. State Commun.* **58**, 739 (1986).
- [47] Y. Nishi, *Jpn. J. Appl. Phys.* **10**, 52 (1972).
- [48] E. H. Poindexter, P. J. Caplan, B. E. Deal, and R. Razouk, *J. Appl. Phys.* **52**, 879 (1981).
- [49] A. Stesmans, J. Braet, J. Witters, and R. F. Dekeersmaecker, *Surf. Sci.* **141**, 255 (1984).
- [50] K. L. Brower, *Semicond. Sci. Technol.* **4**, 970 (1989).
- [51] J. L. Cantin, M. Schoisswohl, H. J. von Bardeleben, N. H. Zoubir, and M. Vergnat, *Phys. Rev. B* **52**, R11599 (1995).
- [52] S. Maekawa and N. Kinoshita, *J. Phys. Soc. Jpn.* **20**, 1447 (1965).
- [53] J. D. Quirt and J. R. Marko, *Phys. Rev. B* **5**, 1716 (1972).
- [54] H. Adhikari, A. F. Marshall, C. D. E. Chidsey, and P. C. McIntyre, *Nano Lett.* **6**, 318 (2006).
- [55] C. B. Jin, J. E. Yang, and M. H. Jo, *Appl. Phys. Lett.* **88**, 193105 (2006).
- [56] H. Jagannathan, M. Deal, Y. Nishi, J. Woodruff, C. Chidsey, and P. C. McIntyre, *J. Appl. Phys.* **100**, 024318 (2006).
- [57] E. Sutter and P. Sutter, *Nano Lett.* **8**, 411 (2008).
- [58] A. B. Greytak, L. J. Lauhon, M. S. Gudiksen, and C. M. Lieber, *Appl. Phys. Lett.* **84**, 4176 (2004).
- [59] T. Hanrath and B. A. Korgel, *Nano Lett.* **4**, 1455 (2004).
- [60] E. Tutuc, J. Appenzeller, M. C. Reuter, and S. Guha, *Nano Lett.* **6**, 2070 (2006).
- [61] J. H. Woodruff, J. B. Ratchford, I. A. Goldthorpe, P. C. McIntyre, and C. D. E. Chidsey, *Nano Lett.* **7**, 1637 (2007).
- [62] N. Fukata, K. Sato, M. Mitome, Y. Bando, T. Sekiguchi, M. Kirkham, J. I. Hong, Z. L. Wang, and R. L. Snyder, *ACS Nano* **4**, 3807 (2010).
- [63] J. G. Connell, K. H. Yoon, D. E. Perea, E. J. Schwalbach, P. W. Voorhees, and L. J. Lauhon, *Nano Lett.* **12**, 199 (2012).
- [64] L. J. Lauhon, M. S. Gudiksen, D. Wang, and C. M. Lieber, *Nature* **420**, 57 (2002).
- [65] R. N. Musin and X. Q. Wang, *Phys. Rev. B* **71**, 155318 (2005).
- [66] J. Xiang, W. Lu, Y. Hu, Y. Wu, H. Yan, and C. M. Lieber, *Nature* **441**, 489 (2006).
- [67] I. A. Goldthorpe, A. F. Marshall, and P. C. McIntyre, *Nano Lett.* **8**, 4081 (2008).
- [68] I. A. Goldthorpe, A. F. Marshall, and P. C. McIntyre, *Nano Lett.* **9**, 3715 (2009).
- [69] J. G. Swadener and S. T. Picraux, *J. Appl. Phys.* **105**, 044310 (2009).
- [70] J.-S. Park, B. Ryu, B. C.-Y. Moon, and K. J. Chang, *Nano Lett.* **10**, 116 (2010).
- [71] L. Li, D. J. Smith, E. Dailey, P. Madras, J. Drucker, and M. R. McCartney, *Nano Lett.* **11**, 493 (2011).
- [72] M. Amato, S. Ossicini, and R. Rurali, *Nano Lett.* **11**, 594 (2011).
- [73] Y. Zhao, J. T. Smith, J. Appenzeller, and C. Yang, *Nano Lett.* **11**, 1406 (2011).
- [74] S. A. Dayeh, J. Wang, N. Li, J. Y. Huang, A. V. Gin, and S. T. Picraux, *Nano Lett.* **11**, 4200 (2011).
- [75] F. Cerdeira, T. A. Fjeldly, and M. Cardona, *Phys. Rev. B* **8**, 4734 (1973).
- [76] K. Arya, M. A. Kanehisa, M. Jouanne, K. P. Jain, M. Balkanski, *J. Phys. C* **12**, 3843 (1979).
- [77] M. Chandrasekhar, H. R. Chandrasekhar, M. Grimsditch, and M. Cardona, *Phys. Rev. B* **22**, 4825 (1980).
- [78] N. Fukata, S. Ishida, S. Yokono, R. Takiguchi, J. Chen, T. Sekiguchi, and K. Murakami, *Nano Lett.* **11**, 651 (2011).
- [79] P. M. Fahey, P. B. Griffin, and J. D. Plummer, *Rev. Mod. Phys.* **61**, 289 (1988).
- [80] L. Sharma, *Defect Diff. Forum* **70-71**, 1 (1990).
- [81] J. S. Cristensen, H. h. Radamson, A. Y. Kuznetsov, and B. G. Svensson, *Appl. Phys. Lett.* **82**, 2254 (2003).
- [82] S. Y. Ma and S. Q. Wang, *Eur. Phys. J. B* **72**, 567 (2009).
- [83] W. C. Jr Dunlap, *Phys. Rev.* **94**, 1531 (1954).
- [84] W. Meer and D. Pommerrenig, *Z. Angew. Phys.* **23**, 369 (1967).
- [85] S. Uppal, A. F. W. Willoughby, J. M. Bonar, A. G. Evans, R. Morris, and M. G. Dowsett, *J. Appl. Phys.* **90**, 4293 (2001).
- [86] S. Uppal, A. F. W. Willoughby, J. M. Bonar, A. G. Evans, N. E. B. Cowen, T. Grasby, R. J. H. Morris, and M. G. Dowsett, *J. Appl. Phys.* **96**, 1376 (2004).
- [87] S. Matsumoto and T. Niimi, *J. Electrochem. Soc.* **125**, 1307 (1978).
- [88] C. O. Chui, K. Gopalakrishnan, P. B. Griffin, J. D. Plummer, and K. C. Saraswat, *Appl. Phys. Lett.* **83**, 3275 (2003).
- [89] T. Canneaux, D. Mathiot, J. P. Ponpon, and Y. Leroy, *Thin Solid Films* **518**, 2394 (2010).
- [90] H. H. Silvestri, H. Bracht, J. L. Hansen, A. N. Larsen, and E. E. Haller, *Semicond. Sci. Technol.* **21**, 758 (2006).
- [91] M. Gavelle, E. M. Bazizi, E. Scheid, P. F. Fazzini, F. Cristiano, C. Armand, W. Lerch, S. Paul, Y. Campidelli, and A. Halimaoui, *J. Appl. Phys.* **104**, 113524 (2008).
- [92] P. Castrillo, R. Pinacho, M. Jaraiz, and J. E. Rubio, *J. Appl. Phys.* **109**, 103502 (2011).
- [93] K. Sakamoto, K. Nishi, F. Ichikawa, and S. Ushio, *J. Appl. Phys.* **61**, 1553 (1987).
- [94] A. S. Grove, O. Leistiko, and C. T. Sah, *J. Appl. Phys.* **35**, 2695 (1964).
- [95] S. M. Hu, *J. Appl. Phys.* **45**, 1567 (1974).
- [96] S. Matsumoto, Y. Ishikawa, and T. Niimi, *J. Appl. Phys.* **54**, 5049 (1983).

- [97] H. J. Gossmann, C. S. Rafferty, H. S. Luftman, F. C. Unterwald, T. Boone, and J. M. Poate, *Appl. Phys. Lett.* **63**, 639 (1993).
- [98] B. Sadigh, T. J. Lenosky, S. K. Theiss, M. J. Caturla, T. D. de la Rubia, and M. A. Foad, *Phys. Rev. Lett.* **83**, 4341 (1999).
- [99] W. Windl, M. M. Bunea, R. Stumpf, S. T. Dunham, and M. P. Masquelier, *Phys. Rev. Lett.* **83**, 4345 (1999).
- [100] P. Alippi, L. Colombo, P. Ruggerone, A. Sieck, G. Seifert, and Th. Frauenheim, *Phys. Rev. B* **64**, 075207 (2001).
- [101] N. Fukata, M. Mitome, Y. Bando, M. Seoka, S. Matsushita, K. Murakami, J. Chen, and T. Sekiguchi, *Appl. Phys. Lett.* **93**, 203106 (2008).